

University of Groningen

## Nanotribology investigations with classical molecular dynamics

Solhjo, Soheil

**IMPORTANT NOTE: You are advised to consult the publisher's version (publisher's PDF) if you wish to cite from it. Please check the document version below.**

*Document Version*

Publisher's PDF, also known as Version of record

*Publication date:*

2017

[Link to publication in University of Groningen/UMCG research database](#)

*Citation for published version (APA):*

Solhjo, S. (2017). *Nanotribology investigations with classical molecular dynamics*. [Thesis fully internal (DIV), University of Groningen]. University of Groningen.

### Copyright

Other than for strictly personal use, it is not permitted to download or to forward/distribute the text or part of it without the consent of the author(s) and/or copyright holder(s), unless the work is under an open content license (like Creative Commons).

The publication may also be distributed here under the terms of Article 25fa of the Dutch Copyright Act, indicated by the "Taverne" license. More information can be found on the University of Groningen website: <https://www.rug.nl/library/open-access/self-archiving-pure/taverne-amendment>.

### Take-down policy

If you believe that this document breaches copyright please contact us providing details, and we will remove access to the work immediately and investigate your claim.

Downloaded from the University of Groningen/UMCG research database (Pure): <http://www.rug.nl/research/portal>. For technical reasons the number of authors shown on this cover page is limited to 10 maximum.

# Appendix A. Sliding contacts of lubricated randomly rough surfaces<sup>\*</sup>

---

## A.1 Introduction

The friction of contacting interfaces is a function of surface roughness, normal load, temperature, sliding velocity, and environmental parameters: e.g., under boundary lubrication, the frictional behavior changes as a function of wettability, viscosity, and density of the applied lubricant, by practically decreasing the possibility of dry (solid/solid) contact. Many atomistic studies of rough contacts adopt simplified sinusoidal shapes for the roughness, and model the interface as that between a deformable surface and a rigid flat; however, as shown in Chapter 5, roughness has a random nature down to the atomic scale. This appendix presents some early results on the frictional behavior of lubricated rough contacts.

## A.2 Simulation Methodology

Figure A1 summarizes the simulation setup and the contact process, which was performed in two phases: normal and sliding contacts. The following sections discuss the details of the simulations.

### A.2.1 Setup

A pair of Gaussian randomly rough surfaces was generated with a root-mean square roughness and correlation length of  $10 \text{ \AA}$  and  $8 \text{ \AA}$ , respectively. These were used for constructing two atomic blocks of fcc-nickel with the (100) lattice planes normal to the  $z$  direction. The solid structure was built with a length of  $40a_0 \cong 14.1 \text{ nm}$  in the lateral directions, with  $a_0 = 3.52 \text{ \AA}$  being the lattice constant of nickel, and a minimum thickness of  $2.5 \text{ nm}$  for each block. Each of the two bodies was divided into three layers: rigid,

---

<sup>\*</sup> This appendix has been originally published in conference abstracts of “TriboUK 2015 (England, April 2015)”, and “The international conference on understanding and controlling nano and mesoscale friction (COSTnanoTribo), (Turkey, June 2015)”.

thermostatic, and free deformable. Moreover, different numbers of n-hexadecane molecules, i.e. 0, 192, 576, and 960, formed a lubricant film. The molecules were modeled through the TraPPE potential energy, while the embedded-atom method potential database developed by Zhou et al. was used for governing the nickel atoms. Also, the Lennard-Jones (LJ) potential was used for calculating the interactions between the non-bonded atoms of the lubricant molecules, as well as the molecules and the substrates. It should be noted that the LJ parameters for nickel were collected from the Shu and Davies database.

The equations of motion were solved using the velocity-Verlet algorithm [38]. Periodic boundary conditions were applied to the lateral directions. The weak coupling thermostat [39] was applied to the thermostat layers to keep the temperature at 300 K.

### A.2.2 Procedure

First, the case of normal contact was studied: the rigid layer of a block was fixed, and the other was moved to apply a pressure of 0.5 kPa. This process was performed for a total simulation time of 3 ns, which was found to be long enough for the potential energy to reach a steady-state. Following normal contact, the rigid layer was moved with a constant velocity of 25 m/s along the  $x$  axis for 3 ns.

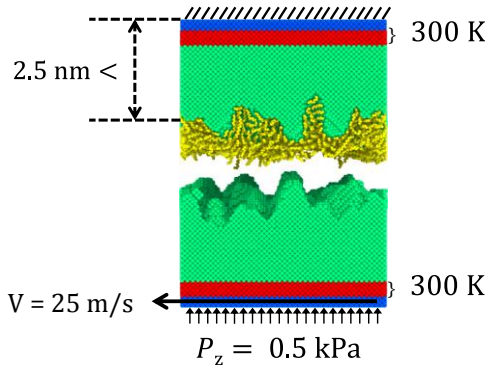


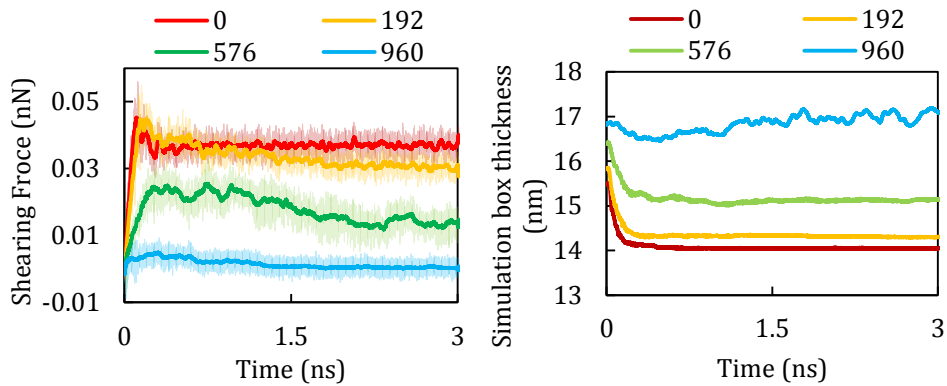
**Figure A1** The atomistic system setup with 960 n-Hexadecane chains, and the details of the contact parameters. It should be noted that the process started with a normal contact, and the sliding contact was simulated only after the potential energy of the system reached a steady-state. In this figure, the atoms of the alkane chains and of the fixed, thermostatic, and Newtonian groups are colored as yellow, blue, red, and green, respectively.

### A.3 Identifying the solid/solid contacting atoms

In lubricated systems, the dry contact may form at different spots if the substrates are not fully covered with the lubricant molecules. These contacting atoms can be identified through defining a contact distance as described in Chapter 3. This method, however, is applicable only for the normal contact phase, in which none of the atoms would leave their original block due to the contact. On the other hand, as soon as the sliding process starts, a number of atoms from each block would stick to the other block, and the system may experience a huge amount of atom transfer. Consequently, the contact distance loses its reliability, because each atom would be recognized as a member of its original substrate, whether it has transferred away from it or not. In order to solve this problem, different approaches can be used based on the mean velocity of atoms [9] or the detection of atom transfer [8], as discussed in Chapter 3. Following the method described therein, a potential cutoff of  $PE_c = -3.965$  eV was defined to identify solid/solid contacting atoms in boundary lubrication. This method needs less computational resources than the method proposed by Spijker et al. [8], and also suffers less from fluctuations compared to the proposed method of Eder et al. [9]. However, there is a main and important limitation in this method: if the system contains different elements, it is highly possible that the method will fail. Chapter 3 provides a detailed review of this method.

### A.4 Results and discussion

Changing the lubricants' volume affected the shearing force as well as the stability of the system. The corresponding results are summarized in Figure A2. Moreover, as illustrated in Table A1, it was found that larger volumes of lubricant localized the dry interactions, and lowered the area of the dry contacting spots, where the atom transfer process occurs. By applying the potential energy cutoff, the non-contacting atoms were identified with ease (see Table A2). The results show that the contacting spots decreased by using larger amounts of lubricant, whether the contact was normal or frictional. Furthermore, the non-contacting area shrunk significantly due to the movement of atoms induced by friction.

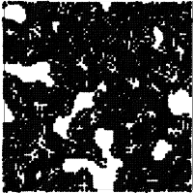
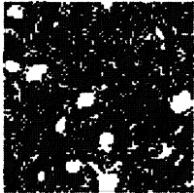
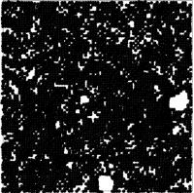
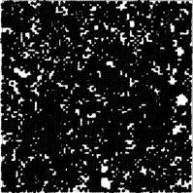
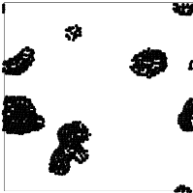
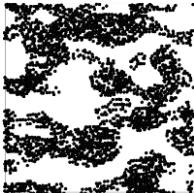
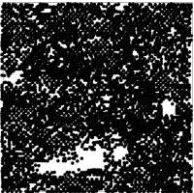
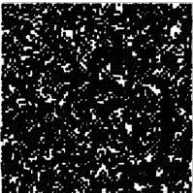


**Figure A2** The effects of the amount of applied lubricant on (left) shearing force, and (right) simulation box thickness.

**Table A1** Side view of the contacting system: the explanation of the colors can be found from the caption of Figure A1. The black strip shows the position of a number of selected atoms before and after the sliding process. Note that the thickness of the system increases for larger amounts of lubricant; the lubricant's chains are not shown.

No. of lubricant molecules	0	192	576	960
Beginning of sliding process				
End of sliding process				

**Table A2** Top view of the non-contacting surface atoms (black dots) via their potential energies. Note that the white area indicates the contacting area.

No. of lubricant molecules	0	192	576	960
Beginning of sliding process				
End of sliding process				

## Appendix B. Contacts with limited adhesion\*

---

### B.1 Introduction

The difficulties in defining the atomic contact distance for, both, adhesive and non-adhesive contacts were discussed in detail in Chapters 2, 3 and 4. It was shown that non-adhesive contacts can be calibrated with the Hertz formula (Chapter 4). On the other hand, adhesive contacts do not need to be calibrated through continuum mechanics solutions: the normalized radial distribution function (RDF) can be used for defining the contact distance; the results would be in agreement with the continuum mechanics solutions, as long as the contact does not deviate from some of the continuum mechanics assumptions, namely that the system is homogenous and that plastic deformation has not been initiated. It should be noted that, in this method, i.e. defining contact distance using RDF, there is one assumption: the atoms of the contacting surfaces are the same as the ones used for calculating the RDF. In other words, if the RDF describes a system composed of a pure element, the contacting surfaces should be pure as well. In real contacts, however, it is unlikely to have fully clean surfaces, for example, due to oxidation. This issue can greatly affect the adhesive forces: in case of oxidation, the adhesion would be lowered. This issue can be addressed differently in the simulations by:

- 1- Introducing different elements into the system. As a result, the contacting surfaces would interact following their potential energies, and the contact distance could be defined using the corresponding RDFs.
- 2- Changing the potential energy values only between the interacting surfaces, in order to artificially incorporate this effect. Using this method, the interacting forces between the contacting surfaces would be different from the forces between the atoms of the substrates. In other words, the contact behaves differently from what the calculated RDFs would suggest.

---

\* This appendix has not been presented/published elsewhere yet.

The second method is more favorable for MD simulations, e.g. see [8, 70, 78, 79, 102], mainly because it would be computationally less expensive than method 1. The incapability of using RDFs for this case, however, makes the analysis of contacts no longer straightforward. In this appendix, the sphere-on-flat elastic contact problem was addressed for the case of limited adhesion. The results were then compared with the JKR theory.

## B.2 A short review of the JKR theory

The JKR theory, among others, was briefly reviewed in Chapter 2. It was developed by incorporating the effect of adhesion in the Hertz theory via an additional pressure distribution [14]:

$$p_{(l)} = p_0 \left(1 - \left(\frac{l}{r}\right)^2\right)^{1/2} - \dot{p}_0 \left(1 - \left(\frac{l}{r}\right)^2\right)^{-1/2}, \quad (\text{B.1})$$

where  $r$  is the contact radius, and  $l$  is the radial distance from the center of the contact, ranging between 0 and  $r$ . The first term of the right hand side is the Hertzian repulsive pressure distribution, and the second term is the pressure distribution responsible for adhesion inside the contact area. For contact between two spheres, the values of  $p_0$  and  $\dot{p}_0$  would be  $2rE^*/\pi R$  and  $\sqrt{2\Gamma E^*/\pi r}$ , respectively.

Johnson et al. [14] solved the pressure distribution for the case of two contacting spheres, and showed that the effectively acting loading force ( $F_{\text{JKR}}$ ) is larger than the normal applied load ( $F_{\perp}$ ):

$$F_{\text{JKR}} = F_{\perp} + F_r \pm (2F_r F_{\perp} + F_r^2)^{1/2}, \quad (\text{B.2})$$

with  $F_r = 3\Gamma\pi R$ . Furthermore, they discussed that the positive sign should be considered for a stable solution. Using this theory, the radius of the contact area can be described as:

$$r = \left( (4R/3E^*) (F_{\perp} + F_r \pm (2F_r F_{\perp} + F_r^2)^{1/2}) \right)^{1/3}, \quad (\text{B.3})$$

which results in a pull-off force of  $F_{\text{po}} = -3/2 \Gamma\pi R$ . Comparing  $F_{\text{po}}$  and  $F_r$ , it can be shown that  $F_r = -2F_{\text{po}}$ . Therefore, (B.2) can be rewritten as:

$$r = \left( (4R/3E^*) \left( F_{\perp} - 2F_{\text{po}} \pm 2(-F_{\text{po}} F_{\perp} + F_{\text{po}}^2)^{1/2} \right) \right)^{1/3}. \quad (\text{B.4})$$

For the case of  $F_{\perp} = F_{\text{po}}$ , the radius of the contact area would be



$$r_{F_{\perp}=F_{po}} = \left( (4R/3E^*)(-F_{po}) \right)^{1/3}. \quad (\text{B.5})$$

Furthermore, the indentation depth  $d$  would be obtained as

$$d = \frac{r^2}{R} - \left( 2 \frac{\pi \Gamma r}{E^*} \right)^{1/2}, \quad (\text{B.6})$$

which can be rewritten by inserting  $F_{po}$  in it as follows:

$$d = \frac{r^2}{R} - 2 \left( -\frac{r F_{po}}{3E^*} \right)^{1/2}. \quad (\text{B.7})$$

Moreover, it can be shown that, for the case of  $F_{\perp} = F_{po}$ , the following holds:

$$d_{F_{\perp}=F_{po}} = -\frac{1}{3} \left( -\frac{3F_{po}}{4E^* \sqrt{R}} \right)^{2/3}. \quad (\text{B.8})$$

### B.3 Simulation Methodology

Two sets of simulations were performed: one for the single asperity contact, and one for the calculation of the work of adhesion. The schematics of the systems are depicted in Figure B1.

The systems were generated from fcc-calcium with a lattice constant of  $a_0 = 5.5884 \text{ \AA}$  [91]. The movements of the deformable atoms were governed by the EAM potential database developed by Sheng et al. for calcium [91]. For the contacting surfaces, the standard LJ potential was used, with  $\varepsilon = 0.21445 \text{ eV}$  and  $\sigma = 3.5927 \text{ \AA}$  [71]; in order to simulate the limited adhesion, however, the depth of the potential well was modified to be  $c\varepsilon$ , with  $c \in \{0, 0.1, 0.2, \dots, 1\}$ . Moreover, a cutoff radius of  $r_{\text{cutoff}} = 2.5\sigma$  was applied to the potential, with the standard GROMACS shift function [121] between a distance of  $r_{\text{shift}} = 2\sigma$  and  $r_{\text{cutoff}}$ ; this shift function assures that there is no jump of energy and force at the cutoff

The equations of motion were solved via the velocity-Verlet algorithm [38]. The temperature of the assigned layers was set to 300 K using Berendsen's thermostat [39]. The crystalline direction of [111] was defined as the  $z$  coordinate direction, and periodic boundary conditions were applied along the lateral directions.

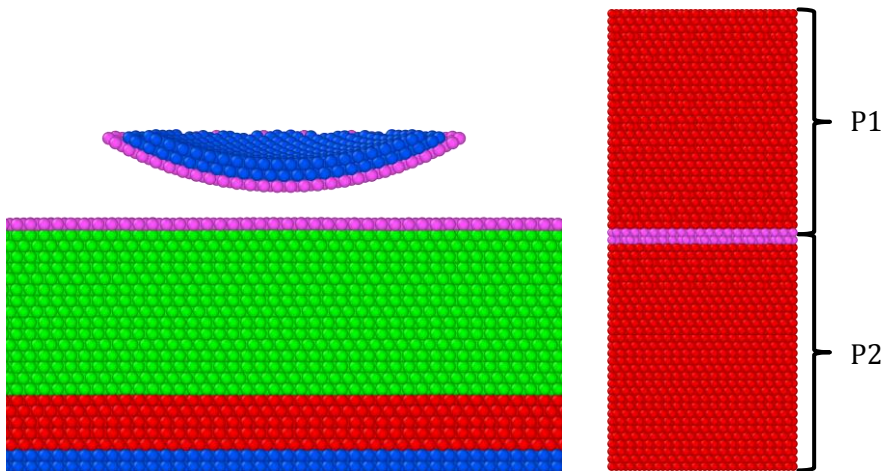


**Figure B1** Side view of (left) the sphere-on-flat contacting system, and (right) the system used for calculating the work of adhesion. In both figures, the colors blue, red, green, and purple indicate the rigid, thermostatic, Newtonian, and surface layers (from bottom to top in the flat body). Also, P1 and P2 indicate the two different parts that were placed side by side as needed for the calculation of  $\Gamma$  (see Chapter 2).

### B.3.1 Single asperity contact

The contact was simulated by moving an atomistic rigid spherical cap with a radius of  $R = 100 \text{ \AA}$  toward an atomically flat substrate with a constant velocity of  $1 \text{ m/s}$ . The initial clearance was set to  $3\sigma$ . Following a relaxation time of  $0.5 \text{ ns}$ , the indenter was moved down (toward the substrate) for  $9 \text{ \AA}$ , and  $5 \text{ \AA}$  away from the substrate afterwards.

### B.3.2 Work of adhesion

The method described in Chapter 2 was used for calculating the work of adhesion. It should be noted that, by setting the value of  $c = 0$ , a system is replicated for which the two sections are far from each other.

## B.4 Results and discussion

### B.4.1 Work of adhesion

Figure B2 shows the work of adhesion as a linear function of  $c$ . Aside from this value, the interacting energy between the surface layers of the contacting parts ( $E_{L1}$ ) was also measured (the purple layers of Figure B1 (b)).

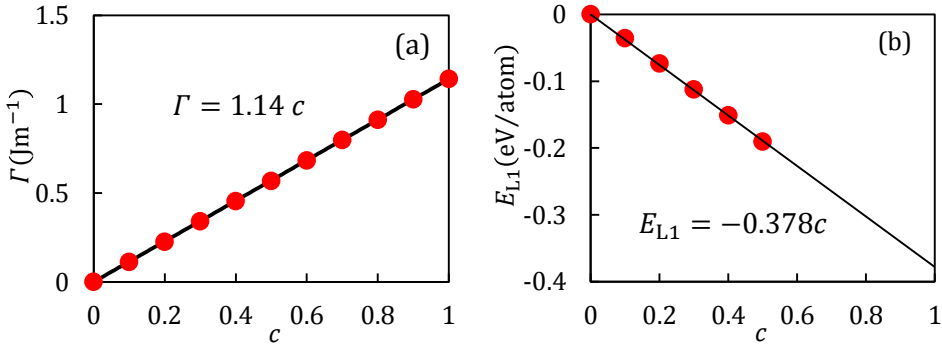


**Figure B2** (a) The work of adhesion, and (b) the interacting energy per atom of the contacting surface layers.

### B.4.2 Overview of the contact results

Figure B3 shows the  $F - d$  curve of the contacting systems with  $c = 0.5$  and  $c = 0.6$ . The results show that the contacting systems with  $c \geq 0.6$  exhibit plastic deformation; therefore, the analyses were limited to the systems with  $0.1 \leq c \leq 0.5$ ; these did not show any plastic deformation or adhesion hysteresis. Table B1 summarizes the measured values of the pull-off forces for each system. By calculating the values of  $\chi = -F_{po}/\pi R\Gamma$ , it can be shown that the systems' contacting behavior tends to the JKR limit (see Figure B4).

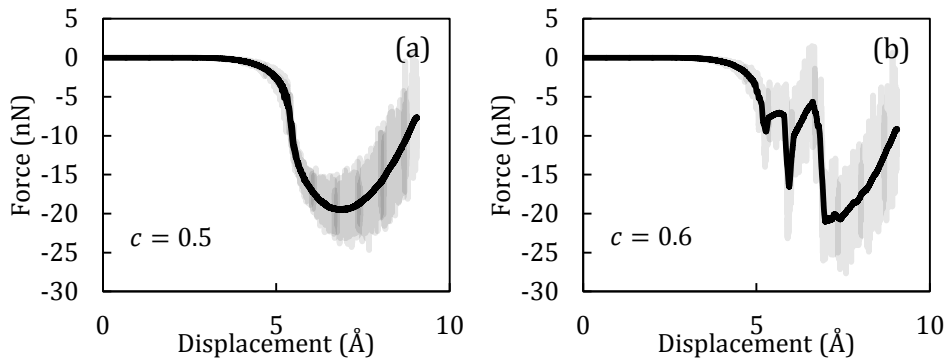


**Figure B3** The normal applied force of the contacting systems with (a)  $c = 0.5$  (for the whole course of loading and unloading), and (b)  $c = 0.6$  (for the movement of the indenter toward the substrate) as functions of displacement. It should be noted that  $d = 0 \text{ \AA}$  points to the initial position of the indenter.

**Table B1** The measured pull-off forces of the simulated contacting systems.

$c$	0.1	0.2	0.3	0.4	0.5
$F_{po}$ (nN)	-3.98	-8.71	-12.64	-16.16	-19.56

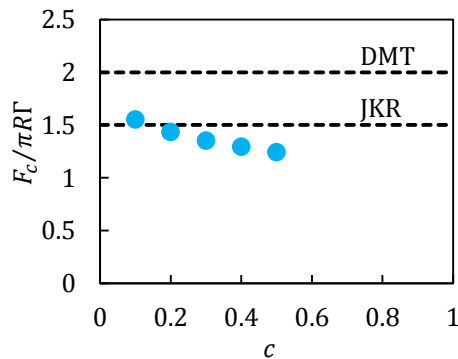


**Figure B4** The comparison between the simulated systems with the limiting cases of JKR and DMT.

### B.4.3 $F - d$ curves

The  $F - d$  curves were calibrated by means of the JKR solution for  $d_{F_{\perp}=F_{p0}}$  using (B.8). This method can calibrate the indentation depth, which is the same as the penetration depth in the continuum mechanics theories: these two parameters are the same, mainly because, in continuum mechanics theories, the contact is defined to start from the moment that the distance between two contacting bodies is zero. At the atomic scale, however, there is always a minimum distance between the centers of atoms. Therefore, these two parameters, namely indentation depth and penetration depth, should be distinguished: the indentation depth is related to the position of the indenter, and the penetration depth is related to the displacement of the deformed substrate. While this value might be inaccessible in experimental setups, it can be easily measured from the simulation.

Figure B5 shows the results for the indentation depths calibrated with the JKR solution for  $d_{F_{\perp}=F_{p0}}$ , the penetration depths measured directly from the simulations, and the JKR solutions calculated from (B.7). The results confirm the applicability of the proposed calibrating method. Moreover, the results show that, while the indentation depth deviates from the JKR solution for distances larger than  $d_{F_{\perp}=F_{p0}}$ , the behavior of the substrate, which was reflected in the penetration depth, was close to the JKR solution.

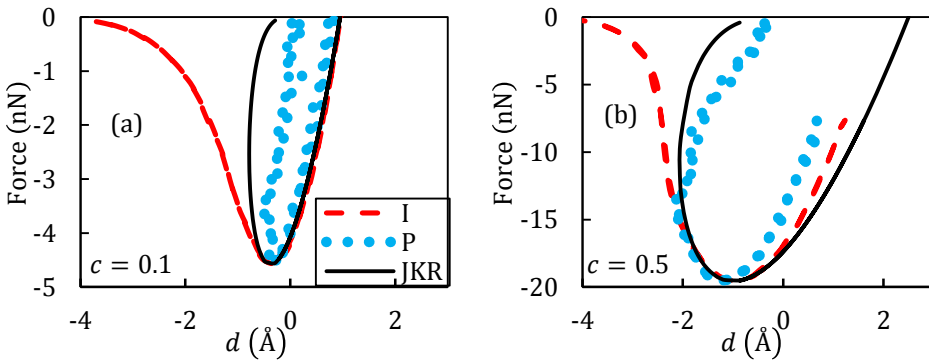


**Figure B5** The force of the systems with (a)  $c = 0.1$ , and (b)  $c = 0.5$  as functions of the calibrated indentation depth (I: red dashed lines) and penetration depth (P: blue dots). The continuous black lines represent the JKR solutions for the contacting systems. It should be noted that the penetration depth values were smoothed using a moving average filter with a span of 5% of the data points.

Also note that the force axes ranges are different.

## B.4.4 The radius of the contact area

In order to calculate the contact radius, the contact area should first be estimated, which can be done with, either, method **B** (counting the contacting atoms), or method **C** (measuring the contact energy), discussed in detail in Chapter 3. It should be noted that the projection of the non-contacting atoms (method **A**) would be inapplicable, due to the limited changes in the potential energy of the contacting atoms. Also, in both methods, the number of the contacting atoms and the contact area were translated via the contact area of an individual calcium atom, which is  $A_a \cong 12.19 \text{ \AA}^2$  (see Chapter 4).

In order to use method **B**, first, a contact distance  $d_c$  should be defined for identifying the contacting atoms. Therefore, as the first step,  $d_c$  needs to be defined and calibrated. This can be done using the JKR theory, or the contact energy.

### B.4.4.1 Method B1: calibration of the contact distance using the JKR theory

The value of  $d_c$  can be calibrated by comparing the simulation results with the JKR theory at pull-off, where the contact radius can be obtained from (B.5). Then, the contact area can be calculated as  $A_{\text{JKR}} = \pi r_{\text{JKR}}^2$ . Dividing this value by  $A_a$ , the reference number of contacting atoms at the pull-off ( $N_{ca,B1}$ ) can be estimated. Comparing this value with the simulation results at the pull-off, the contact distance can be defined such that the number of the contacting atoms matches the calibrating value of  $N_{ca,\text{JKR}}$ .

### B.4.4.2 Method B2: calibration of the contact distance using the contact energy

The calibration of  $d_c$  at the pull-off can be done by considering the interacting energy of the surface atoms of the contacting systems ( $E_{L1,C}$ ), which was calculated from surface layer (purple) atoms in Figure B1. The reference value of  $N_{ca,E}$  would be  $N_{ca,B2} = E_{L1,C} \times E_{L1}$  at the pull-off, with  $E_{L1}$  reported in Figure B2(b). The rest of the procedure would be the same as described in section B.4.4.1.

### B.4.4.3 Method C: measuring the contact radius using the contact energy

This method can be directly applied via  $N_{ca,C} = E_{L1,C} \times E_{L1}$  through all the simulation, and not only at the pull-off.

### B.4.4.4 Comparison between the utilized methods

The results of the three described methods are shown in Figure B6. These show that, by calibrating the contact distance with the JKR solution at the pull-off, the system can be well described by the JKR theory for contact above the pull-off. This stability was investigated, and reported below; however, first, it is interesting to compare the results of method B1 with methods B2 and C. As Figure B6 (a) shows, the JKR theory underestimated the contact area for the whole range of the contact; however, Figure B6 (b) shows that, as  $c$  increases, the contact area tends toward the JKR solution. When analyzing all systems, it was found the simulation results were in a good agreement with the JKR solution for  $0.3 \leq c \leq 0.5$ .

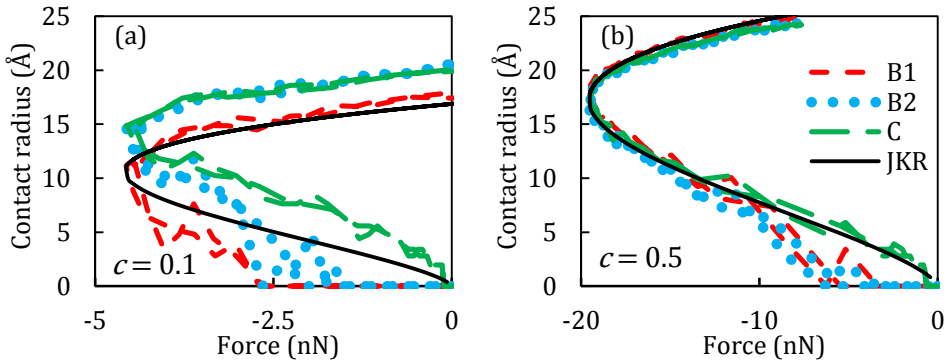


**Figure B6** The calculated contact radii for the systems with (a)  $c = 0.1$ , and (b)  $c = 0.5$  using the three described methods, in comparison to the JKR solution. Note that the force axes ranges are different.

Another important result, presented in Figure B6, is the difference between the contact radius for contact beyond the pull-off: methods B1 and B2 measured contact radii of zero for the initial/ending stages of the contact, while method C and the JKR solution yield non-zero contact radii for any non-

zero force. Considering method C to be the correct solution for the simulated systems, the contact distance was estimated for the whole simulation using the reference number of contacting atoms  $N_{ca,C}$ . The results for two of the systems with  $c = 0.1$  and  $c = 0.5$  are shown in Figure B7. As the results indicate, the contact distance changes for the initial/ending stages of the contact, i.e. the contact beyond the pull-off. The contact distance, however, would be constant away from the pull-in/pull-off stages. This indicates that the pull-off is an appropriate position for the calibration of the contact distance, because the value of  $d_c$  would not change for larger normal loads. This behavior is true whether the calibration was done using the JKR theory (method B1), or the contact energy (method B2). This is the reason for the stability of the simulation results with the JKR solution.

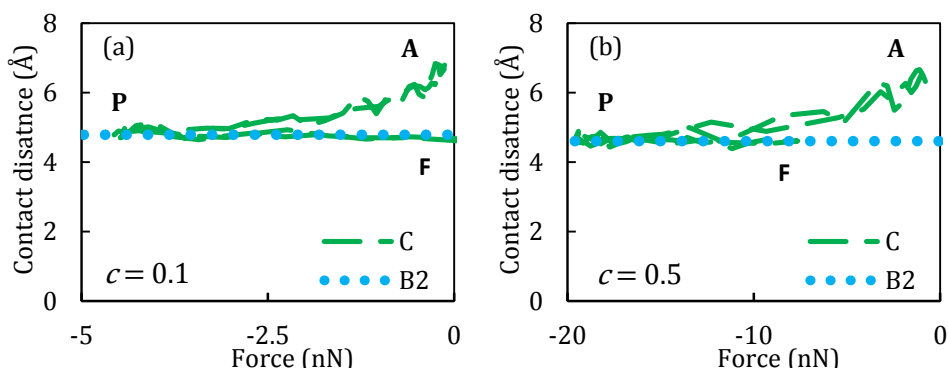


**Figure B7** The calculated contact distances for the systems with (a)  $c = 0.1$ , and (b)  $c = 0.5$  using the reference number of contacting atoms measured from method C ( $N_{ca,C}$ ). Point A indicates the inception of contact. Then, the force decreases due to the adhesion, until the system reaches point P. Following this point, the repulsive force results in an increase in the total force, up to point F for the simulated system. The results show that the contact distance does not change while the system is between points P and F.



## Appendix C. Contact pressure dependence on the interacting potential\*

---

The pressure distribution of a contact between a rigid indenter and a deformable substrate depends on the applied interacting potential energy. In Chapter 4, the non-adhesive interactions were modelled by applying the non-adhesive part of the LJ potential; however, this was not the only solution. One can model short-range repulsion via the standard LJ potential, by cutting the potential at its minimum, and adding a constant to assure that the interacting force and energy go smoothly to zero at the cutoff. Figure C1 shows the contact pressure distribution for two cases of interacting potentials. Moreover, the interacting potential energy affects the indenter's responses; these effects are summarized in Table C1 and Figure C2.

The results show that, as the interacting potential energy approximates a hard-wall interaction, the fitted values of  $E^*$  increase to the bulk value of  $E^* = 28.57$  GPa with a higher rate; however, for larger indentation depths, i.e.  $d > 4$  Å in this study, the indenters' responses were found to be very similar, and independent from the interacting potential energy.

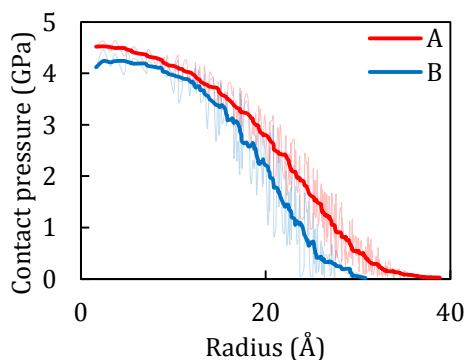


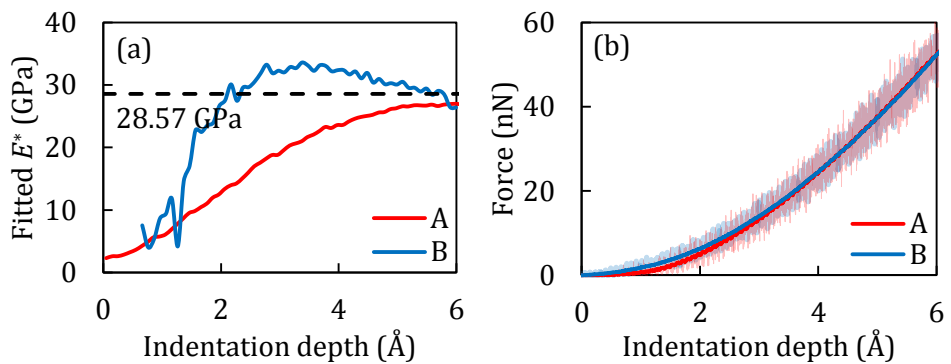
**Figure C1** The interfacial contact pressure distribution between a rigid indenter of  $R = 100$  Å and a deformable body. The non-adhesive contact was modeled with (A) the repulsion part of the LJ, and (B) cutting and shifting the LJ at its minimum.

---

\* This is an appendix to Chapter 4.

**Table C1** The values of the contact pressure threshold ( $P_c$ ), contact distance ( $d_c$ ), and the corrective shifts of displacement ( $\delta_d$ ) and force ( $\delta_F$ )

Case	$P_c$ (GPa)	$d_c$ (Å)	$\delta_d$ (Å)	$\delta_F$ (nN)
A	1.335	4.964	5.721	0.620
B	1.190	4.826	6.786	0.002

**Figure C2** (a) The fitted values of  $E^*$ , and (b) the force-indentation depth curves for cases A and B.

## Appendix D. Contact-induced stress fields\*

---

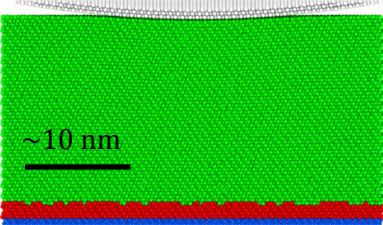
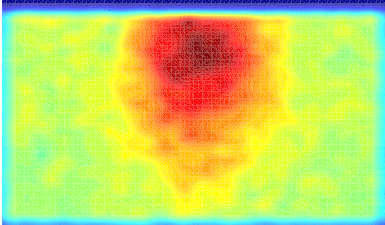
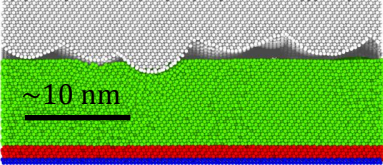
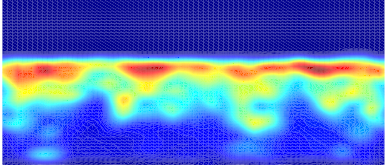
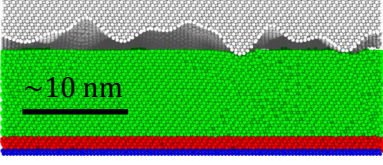
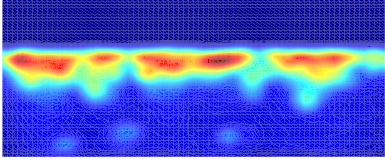
Applying periodic boundary conditions (PBCs) along the desired directions is a classical method in MD simulations used to avoid the edges imposed by the finite size of the simulated system. In some systems, however, such as the ones investigated in chapter 4, PBCs are not applicable in the directions normal to a free surface. Consequently, the system behavior, including its mechanical response, could be affected by the finite system size in the directions where PBCs are not applied.

In the study of Chapter 4, an atomistic fixed layer providing the necessary mechanical support to the deformable bodies was used along the plane parallel to the free surface. As a result, the mechanical response of the systems would be affected by that fixed layer if the stress fields crossed the deformable body and reached the fixed layer. Allowing for this behavior could be relevant for thin layers, but not for bulk materials as was intended in the study. In order to remove this boundary effect, one may simulate the system using Green's function MD (GFMD) [11], smartblock MD [12], or by coupling MD with other techniques such as the finite element method (FEM), e.g. via the Atoms-to-Continuum package of LAMMPS; given sufficient computational resources, it is also possible to simulate an extremely large system using classical MD [122]. In this work, classical MD was used, and the results were collected up to the point before which the stress fields were affected by the fixed layer. This condition was tested through the calculation of the contact influenced stress values ( $CS$ ) by subtracting the stress values of each atom at the end of the equilibration process ( $S_{eq}$ ) from their corresponding value at each time step ( $S_t$ ), i.e.  $CS_t = S_t - S_{eq}$ , where  $CS_t$  indicates the values of  $CS$  at time step  $t$ . Then, the system was meshed along one of the lateral axes, and the maximum values of  $CS$  were collected. By examining these data, it was possible to identify the instances at which the stress fields reached the fixed layers. Table D1 shows the stress fields of a number of the contacting systems, at the last step of data extraction.

---

\* This is an appendix to Chapter 4.

**Table D1** The representation of the atomic structures of the contacting systems (normal to the  $x$  axis), and their contact-induced stress fields. The atoms are represented in the left column as circles with different colors: fixed (blue), thermostatic (red), non-constrained (green), and the indenter as white. The right column shows the projection of the maximum values of the contact induced stress ( $CS$ ) values on a plane normal to the  $x$  axis: dark blue indicates the minimum of value of 0, and dark red indicates the maximum of the values, which was 0.9 GPa, 8.5 GPa, and 10.2 GPa, for the cases of single asperity, GW rough surface, and random rough surface, respectively.

	Atomic structure	Contact induced stress field
Single asperity (1000 Å)		
GW-type rough surface		
Randomly rough surface		

## Appendix E. The exponent of PSD\*

---

For self-affine fractal profiles, the slope of the PSD would be [123]

$$\beta = -(2H + D_S), \quad (\text{E.1})$$

where  $H$  is the Hurst exponent, and  $D_S$  is the spatial dimension of the projected fractal, i.e.  $D_S = 2$  for a fractal surface and  $D_S = 1$  for a fractal line. The Hurst exponent describes the raggedness of the profile, with a lower value leading to a rougher profile. The value of the Hurst exponent is bounded as  $0 < H < 1$ . Considering the range of the Hurst exponent, one may conclude that  $\beta \in (-2, -4)$  for a fractal surface. The definition of the PSD in the form of (5.2), however, does not apply such a restriction on the values of  $\beta$ . On the other hand, if  $\beta$  exceeds the abovementioned limitation, the value of  $H$  would vary outside the range of  $(0,1)$ ; therefore,  $H$  loses its general meaning of the Hurst exponent [124]. This is the main reason why the PSD exponent is not expressed in terms of  $H$  or  $D_S$  in the current study.

---

\* This is an appendix to Chapter 5.

## Appendix F. The spectral moments of PSD\*

---

The spectral moments of the PSD can be calculated from [125]

$$m_n = A_n \int_0^{+\infty} q^{1+n} C(q) dq, \quad (\text{F.1})$$

with

$$A_n = \int_0^{2\pi} (\cos \omega)^n d\omega. \quad (\text{F.2})$$

For  $n = 0, 2,$  and  $4,$   $A_n$  equals  $2\pi, \pi,$  and  $3\pi/4,$  respectively. Considering the definition of  $C(q)$  for  $q_L \leq q \leq q_S$  based on (5.2), (F.1) can be solved and reformulated as follows:

$$m_n = A_n C_0 q_r^{2+n} I_n, \quad (\text{F.3})$$

with

$$I_n = \frac{1 - M_L^{2+n}}{2 + n} - \frac{1 - M_S^{2+n+\beta}}{2 + n + \beta}, \quad (\text{F.4})$$

where  $M_L = q_L/q_r,$  and  $M_S = q_S/q_r.$  These formulae are important for the generation of rough surfaces; a rough surface can be generated by solving (5.1), where the values of  $h(\mathbf{q})$  should be converted from the values of  $C(\mathbf{q})$  in the form of (5.2). In order to solve (5.2), the values of  $q_L, q_r, q_S, \beta,$  and  $C_0$  need to be defined beforehand. The values of these variables can be assigned arbitrarily, provided they do not violate the conditions of  $q_L < q_r < q_S, \beta < 0,$  and  $C_0 > 0.$  The value of  $C_0,$  however, can be defined such that the generated surface will possess a specific spectral moment. Considering that  $m_0 = \sigma_{\text{rms}}^2$  [104], and  $m_2 = \frac{1}{2} \bar{g}^2$  [126], the parameter  $C_0$  can be defined as  $C_0 = \sigma_{\text{rms}}^2 (A_0 I_0 q_r^2)^{-1}$  and  $C_0 = \frac{1}{2} \bar{g}^2 (A_2 I_2 q_r^4)^{-1},$  respectively. In order to generate a surface with given values of  $\sigma_{\text{rms}}$  and  $\bar{g},$  however,  $C_0$  will need to have a unique solution, resulting in a distinctive roll-off wavenumber of  $q_r = (\bar{g}/\sigma_{\text{rms}}) \sqrt{I_0/I_2},$  which cannot be solved analytically. Therefore, in this study,  $C_0$  was estimated based on the PSD's zeroth moment, in order to generate rough surfaces with a specific value of  $\sigma_{\text{rms}}.$

---

\* This is an appendix to Chapter 5.

## Appendix G. The mean gradient for a limiting case of nominally flat rough $\{100\}$ planes in an fcc structure\*

---

For an atomistic nominally flat rough surface, a limiting case would be a saw-tooth rough surface, with every other atom removed along each of the lateral directions. In the surface analysis methods adapted in this work, the atomistic rough surfaces were projected on a uniformly gridded plane. The estimated surface for the abovementioned limiting case is shown in Figure G1. It can be shown that the local gradient on each grid point is  $\sqrt{2}$ . Consequently, the mean gradient of this limiting case would be  $\sqrt{2}$ .

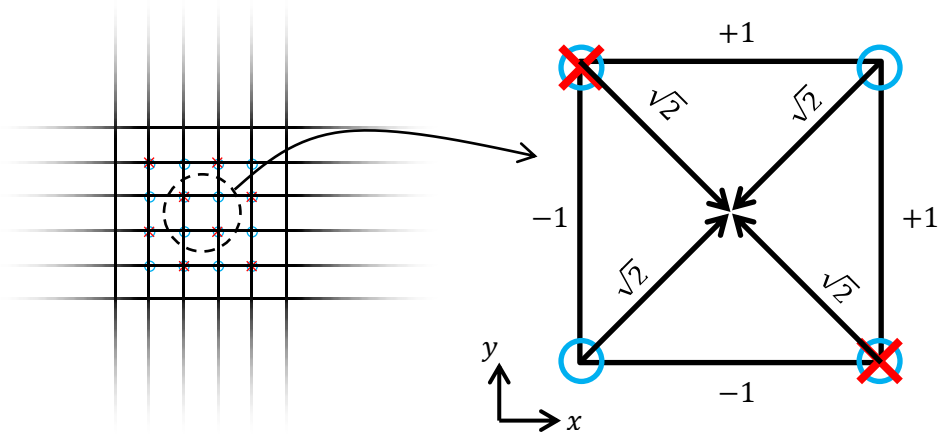


**Figure G1.** (Left) The uniformly gridded plane for the limiting case of an atomistic nominally flat rough surface along the  $\{001\}$  planes of an fcc structure, where every other atom is removed along each direction of  $x$  and  $y$ . Note that no grid was assigned for the faced-centered atoms in the surface analysis of the current work. (Right) A selected grid of the saw-tooth rough surface. The numbers on the edges indicate the calculated slopes along the  $x$  and  $y$  axes. The numbers on the arrows indicate the local gradients at each grid point.

---

\* This is an appendix to Chapter 5.

## Appendix H. Roughness of molten gold due to capillary waves\*

---

The interface undulation between any two fluids can be described by capillary wave theory; see [127] for a short review, and [128] for a deep discussion on the applicability of this theory in MD simulations. While this theory is most relevant for interfaces between fluids, one may argue that it is still applicable for the cases studied in this research, i.e. free surfaces. In capillary wave theory, the thermally excited height fluctuation spectrum  $h_{\text{CW}}(q)$  of an isotropic crystallographic surface can be expressed by:

$$\langle |h_{\text{CW}}(q)|^2 \rangle = \frac{k_B T}{\gamma L^2} q^{-2}, \quad (\text{H.1})$$

where  $k_B$  is the Boltzmann constant, and  $\gamma$  is the surface energy of the free surface expressed in the dimensions of energy over area. Considering the relation  $C(q) = (L/2\pi)^2 \langle |h(q)|^2 \rangle$  (see section 5.2), the power spectral distribution of the thermally agitated capillary waves can be written as

$$C_{\text{CW}}(q) = \frac{1}{4\pi^2} \frac{k_B T}{\gamma} q^{-2}. \quad (\text{H.2})$$

The RMS roughness of the thermally agitated capillary waves can be obtained from  $m_0$  (see Appendix F) to be

$$\sigma_{\text{rms,CW}} = \left( \frac{1}{2\pi} \frac{k_B T}{\gamma} \ln \left( \frac{L}{\delta} \right) \right)^{0.5}. \quad (\text{H.3})$$

Therefore, the total RMS roughness of the surface can be estimated as

$$\sigma_{\text{rms}} = \sqrt{\sigma_{\text{rms},0}^2 + \sigma_{\text{rms,CW}}^2}. \quad (\text{H.4})$$

Considering (H.3) and the proportionality of  $\sigma_{\text{rms,CW}} \propto \sqrt{T}$ , one may argue that the roughness would be higher as the equilibration temperature increases. This would be in accord with the reported results in section 5.5.5.

As the temperature rises, the material softens and cannot withstand the local stresses due to the initial surface roughness, as is particularly visible for the case of  $T = T_m$ ; however, the generated capillary waves do not allow the

---

\* This is an appendix to Chapter 5.



surface to have a roughness parameter of  $\rho = 0$ . In order to estimate the roughness parameter of the free surface at the melting point, one can assume that the surface roughness is solely due to capillary waves. Therefore, the RMS roughness can be calculated via (H.3). Moreover, the mean gradient can be calculated from  $m_2$  (see Appendix F) to be

$$\bar{g}_{CW} = \left( \pi \frac{k_B T}{\gamma} (\delta^{-2} - L^{-2}) \right)^{0.5}. \quad (\text{H.5})$$

Furthermore, the autocovariance function of the power spectral distribution in the form of (H.2) can be calculated using the zero-order Hankel transform of  $C(q)$ , which results in

$$\text{var}(r) = \frac{1}{2\pi} \int_{q_L}^{q_S} C(q) J_0(qr) q dq, \quad (\text{H.6})$$

where  $J_0$  is the zero-order Bessel function of the first kind. Then, the autocorrelation function can be calculated as  $R(r) = \text{var}(r)/\text{var}(\delta)$ .

For the simulated material, the melting point and the (100) surface energy are 1281 K and  $1.225 \text{ J/m}^2$ , respectively [91]. Inserting these values into (H.3), (H.5), and (H.6), yields values for the RMS roughness, mean gradient, and lateral correlation length of  $\sigma_{\text{rms,CW}} = 0.6a_0$ ,  $\bar{g}_{CW} = 0.5$ , and  $\zeta_{CW} = 4.7a_0$ , respectively. It should be noted that the lateral correlation length was estimated from the numerical solution of (H.6) (see Figure H1). Thus, the roughness parameter of the molten system can be calculated as  $\rho_{CW} \cong 0.07$ , which is very close to the measured value of  $\rho \cong 0.05$  for the system at the melting point (see section 5.5.5).

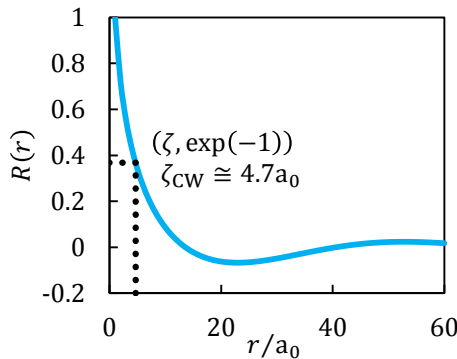


**Figure H1** The autocorrelation function of the thermally agitated capillary waves on a free surface of a gold substrate at the melting point.